N O T I C E

THIS DOCUMENT HAS BEEN REPRODUCED FROM MICROFICHE. ALTHOUGH IT IS RECOGNIZED THAT CERTAIN PORTIONS ARE ILLEGIBLE, IT IS BEING RELEASED IN THE INTEREST OF MAKING AVAILABLE AS MUCH INFORMATION AS POSSIBLE

NASA Technical Memorandum 81236

USAAVRADCOM TR 80-A-12

Transonic Rotor Noise — Theoretical and Experimental Comparisons

F. H. Schmitz and Y. H. Yu

November 1980

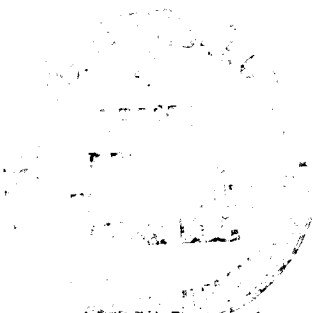

National Aeronautics and Space Administration

United States Army Aviation Research and Development Command

NASA Technical Memorandum 81236

USAAVRADCOM TR 80-A-12

Transonic Rotor Noise — Theoretical and Experimental Comparisons

F. H. Schmitz
Y. H. Yu, Aeromechanics Laboratory
AVRADCOM Research and Technology Laboratories
Ames Research Center, Moffett Field, California

NASA
National Aeronautics and
Space Administration

Ames Research Center
Moffett Field, California 94035

United States Army
Aviation Research and
Development Command
St. Louis, Missouri 63166

TRANSONIC ROTOR NOISE — THEORETICAL AND EXPERIMENTAL COMPARISONS

F. H. Schmitz and Y. H. Yu
Aeromechanics Laboratory
U.S. Army Research and Technology Laboratories (AVRADCOM)
Ames Research Center, NASA
Moffett Field, California, 94035 U.S.A.

ABSTRACT

Two complementary methods of describing the high-speed rotor noise problem are discussed. The first method uses the second-order transonic potential equation to define and characterize the nature of the aerodynamic and acoustic fields and to explain the appearance of radiating shock waves. The second employs the Ffowcs Williams and Hawkings equation to successfully calculate the acoustic far-field. Good agreement between theoretical and experimental waveforms is shown for transonic hover tip Mach numbers from 0.8 to 0.9.

1. INTRODUCTION

It is now well known that linear acoustic theory fails to correlate with many features of measured transonic rotor noise. In particular, linear theory does not predict measured acoustic pressure levels or waveforms of rotating blades operating with transonic flow in the tip region (Refs. 1-5). The discrepancy, in level and waveform, is particularly large for helicopter rotors that use relatively thick airfoil sections (as compared with propellers) operating at high Mach numbers. As a result, large transonic disturbance fields alter and enhance the radiated acoustic signature, making high-speed rotor compressibility noise an important and practical research problem.

Until recent years, the theoretical approaches of rotor noise utilized the "acoustic analogy" of Lighthill (Ref. 6). Ffowcs Williams and Hawkings (Ref. 7) extended the analogy to allow for relative motion between the acoustic sources and an observer, yielding an integral equation that describes the resulting noise. This equation was refined for eventual numerical computation by many authors, most notably those of References 8 and 9. Unfortunately, the helicopter rotor problem is so complex geometrically that an exact "acoustic analogy" was not initially attempted. Instead, the governing equations were linearized and the resulting integrals were numerically evaluated.

Although the success of the linear model at low Mach numbers can still be debated, its success at transonic tip Mach numbers is quite limited (see Fig. 1). Neither the amplitude nor the shape of the far-field acoustic disturbance is accurately predicted. In fact, although a radiating discontinuity (shock) was experimentally measured, linear theory cannot, to any extent, account for this phenomenon. Similar discrepancies have been confirmed by tests with both model and full-scale helicopters in high-speed forward flight (Refs. 1, 10).

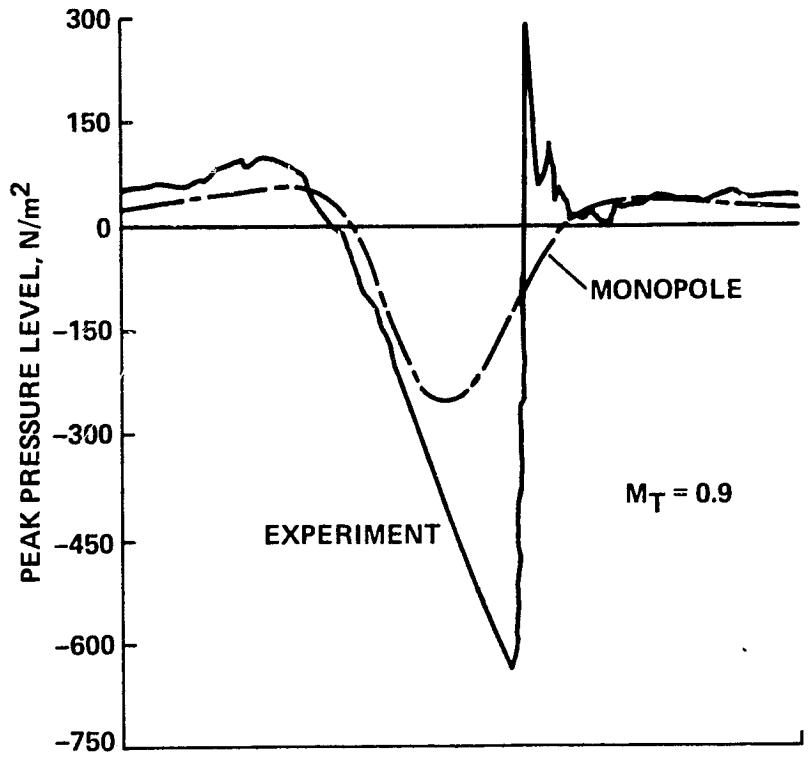

Figure 1. Comparison of theory and experimental pressure-time history, in-plane, r/D = 1.5, M_{tip} = 0.9. (Adapted from Ref. 2).

Realizing this, several researchers have set about to capture the important nonlinear aspects of the high-speed rotor problem (Refs. 1, 11-13). Two different but fundamentally similar approaches have been taken: (1) nonlinear "quadrupole" terms have been re-incorporated into the "acoustic analogy" formulation as additional source terms; and (2) a nonlinear potential equation has been formulated for the acoustic radiation of rotors.

In this paper, we compare and highlight the differences and similarities of both methods. The potential formulation will first be used to help explain some of the more interesting experimental features of the nonlinear flow field surrounding the blade. Then the acoustic analogy approach will be discussed and quadrupole sources will be used to help predict the resulting noise field. Finally, the results will be critically compared with specially run tests to highlight the promise or failings of the acoustic analogy approach and to explain, in simple physical terms, how sound is radiated by a rotor with transonic tip velocities.

2. THE POTENTIAL EQUATION AND ITS IMPLICATIONS

The acoustic radiation of an isolated rotor hovering at transonic tip Mach numbers is considered in this paper. The more difficult problem of high-speed forward flight is deferred until the steady transonic and acoustic features of the hovering problem have been identified. Assuming constant specific heats and weak shocks (i.e., negligible entropy increases), the classical potential equation is:

$$\frac{\partial^2\phi}{\partial t^2} - a^2\,\nabla^2\phi + 2\,\text{grad}\phi \cdot \text{grad}\,\frac{\partial\phi}{\partial t}$$

$$+ \frac{1}{2}\,\text{grad}\phi \cdot \text{grad}[(\text{grad}\phi)^2] = 0 \qquad (1)$$

where ϕ represents the velocity potential and a is the local speed of sound. This nonlinear, time-dependent equation is written in a space-fixed coordinate system; however, the aerodynamics of a hovering rotor are basically steady when viewed from a blade-fixed reference frame. Therefore, following the work of Isom (Ref. 11) the governing potential equation can be transformed to blade-fixed cylindrical coordinates and expanded to second-order, yielding

$$\left\{\omega^2 - \frac{a_0^2}{r^2} - (\gamma+1)\,\frac{\omega}{r^2}\,\phi_\theta\right\}\phi_{\theta\theta} - 2\omega\phi_r\phi_{r\theta} - 2\omega\phi_z\phi_{z\theta}$$

$$= \left\{a_0^2 + (\gamma-1)\omega\phi_\theta\right\}\left(\phi_{rr} + \frac{\phi_r}{r} + \phi_{zz}\right) \qquad (2)$$

where

ω = angular rotation rate
a_0 = undisturbed speed of sound
r = radial distance from the axis of the cylindrical coordinate system
γ = ratio of specific heats

This nonlinear but steady second-order partial differential equation governs the acoustic as well as the transonic behavior of the hovering rotor. At the present time, no closed-form solutions to this equation exist. A procedure adopted by some researchers is to numerically solve limited regions of the aerodynamic flow field (Refs. 14, 15). Others (Ref. 11) have chosen to solve the nonlinear acoustic far-field, using weak-shock theory (Ref. 16). As we shall see, neither is a completely satisfactory solution, for the nonlinear aerodynamic and acoustic fields are interwoven.

The choice of a cylindrical coordinate system whose axis is aligned with the rotor is sketched in Figure 2. An observer riding in this coordinate system sees a free-stream velocity that increases linearly from zero at the origin to ωr at r. As indicated, this increasing free-stream velocity continues out past the tip of the rotor; it will be shown to be important to many of the arguments to come.

Before attempting to solve Equation (2), it is instructive to follow the approach of References 11 and 12 and explore the behavior of the governing equation. It is known from the theory of partial differential equations that the coefficient of $\phi_{\theta\theta}$ governs the general character of the potential equation. For when

$$A \equiv \omega^2 - \frac{a_0^2}{r^2} - (\gamma+1)\,\frac{\omega}{r^2}\,\phi_\theta \qquad (3)$$

< 0 : elliptic behavior

> 0 : hyperbolic behavior

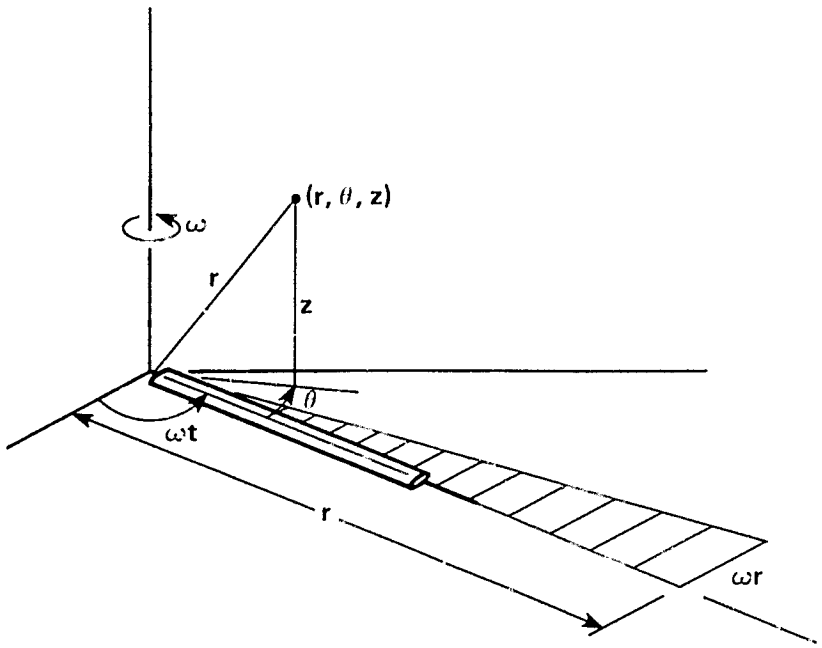

Figure 2. Cylindrical coordinate system.

However, A takes a more recognizable form after some further manipulation:

$$A = \omega^2 - \frac{a_0^2}{r^2} - \frac{(\gamma - 1)\omega}{r^2}\phi_\theta - \frac{2\omega}{r^2}\phi_\theta \tag{4}$$

Using the energy equation, this becomes

$$A = \omega^2 - \frac{a^2}{r^2} - \frac{2\omega\phi_\theta}{r^2} \tag{5}$$

Defining $U_\infty = \omega r$, $\phi_\theta = -ur$, we obtain

$$A = -\frac{a^2}{r^2}\left\{1 - \frac{(U_\infty + u)^2}{a^2} + \frac{u^2}{a^2}\right\} \tag{6}$$

The last term in the brackets of Equation (6) can be neglected. It is second order to A and a third-order correction to the second-order potential equation. If we now define

$$M_\ell \equiv \frac{U_\infty +}{a} = \text{local Mach number},$$

the coefficient of $\phi_{\theta\theta}$ (Eq. (6)) becomes

$$A = -\frac{a^2}{r^2}(1 - M_\ell^2) \tag{7}$$

We have shown that the general behavior of the second-order transonic potential equation is governed by the local Mach number of the flow. If

$M_\ell < 1.0$, then $A < 0$ and the governing equation is elliptic. In this case, no wave-like structure is possible. However, if $M_\ell > 1.0$, then $A > 0$ and the governing nonlinear partial differential equation is hyperbolic. Then, characteristics are formed along which disturbances can propagate in a wave-like manner. It is also important to realize that the local Mach number M_ℓ is dependent on the free-stream velocity ωr, the local speed of sound a, and the local perturbation velocity, $u = -\phi_\theta/r$. Each contribution is separately identifiable in Equation (6).

These ideas are quite useful when one is attempting to interpret the experimental results of Reference 2. In that sequence of experiments, a 1/7-scale twisted and untwisted UH-1H model rotor (NACA 0012 airfoil) was run in an anechoic hover chamber at near zero thrust at high subsonic tip Mach numbers. In-plane acoustic signatures were measured and stationary hot-wire measurements of the local perturbation field (u) surrounding the blade were made. A phenomenon labeled "delocalization" was observed in this experiment as the hover free-stream tip Mach number was increased above 0.88. Shock waves on the rotor suddenly "delocalized" and radiated to the acoustic far-field. The measured far-field acoustic signature transitioned from a near symmetrical triangular pulse shape to a distinct sawtooth character — confirming the existence of a radiating shock wave (Fig. 3).

The connection between the phenomenon of delocalization and the change in equation type has been suggested in References 11 and 13 and reported in Reference 12, based on a numerically calculated local transonic flow field. In the following paragraphs, the relationships are experimentally confirmed and are shown to depend on the local Mach number of the flow. Three distinct cases are considered: $M_{tip} = 0.85$, $M_{tip} = 0.88$, and $M_{tip} = 0.90$. Some degree of graphical freedom is taken in the interest of presenting a clear sketch of the basic relationships involved. The data are the same as those reported in Reference 17, but are expanded upon here. In the figures that follow, the top views are sketches of events pieced together with limited experimental data, and the aft views are, for the most part, interpolations of experimental data.

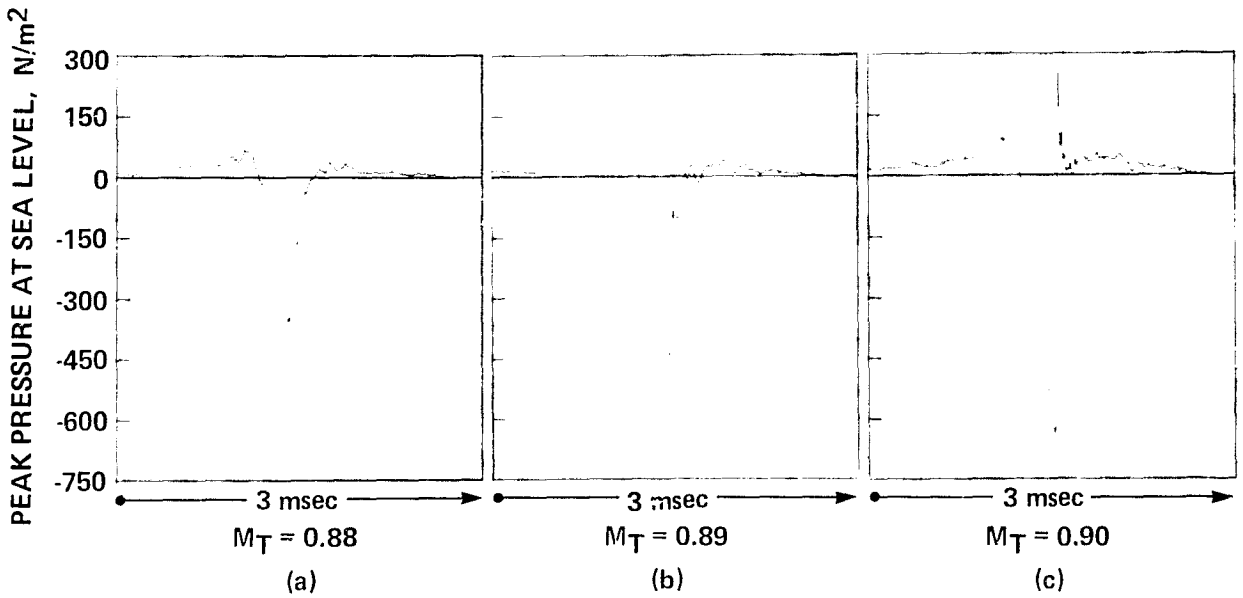

Figure 3. Waveform transition; the development of a radiating discontinuity, in-plane, $r/D = 1.5$, $M_{tip} = 0.9$.

Figure 4 depicts the top and aft views of a rotor operating at a free-stream tip Mach number (M_{tip}) of 0.85. A locally supersonic region exists near the tip of the rotor. For this region $M_\ell = (\omega r + u)/a > 1.0$, even though $\omega r/a_0$ all along the blade span is less than 0.85. The hyperbolic nature of this pocket of supersonic flow is a result of local aerodynamic nonlinearities (i.e., changes in the local speed of sound a, and local perturbation velocity, u). Surrounding this locally supersonic flow is a subsonic flow region, $M_\ell < 1.0$, in which the governing potential equation is elliptic. No wave-like behavior is possible through this compressible elliptic region. However, as r increases beyond the tip of the blade, M_ℓ again becomes greater than 1 because of the linearly increasing free-stream velocity field of the blade-fixed cylindrical coordinate system. For this region $u \approx 0$, $a \approx a_0$, so

$$M_\ell \approx \frac{\omega r}{a_0} > 1.0$$

The surface where this first happens has been called the sonic cylinder (Refs. 11, 13). At radii larger than the sonic cylinder, the equation again becomes hyperbolic, and wave-like propagation is certain. The acoustic implications of this 0.85 case begin in the hyperbolic pocket of flow near the blade tip. Wave-like disturbances in this region terminate on the boundary of an elliptic region where they no longer propagate in characteristic directions. The wave-like character of the inner pocket is thus broadened as information passes through the elliptic region to the sonic cylinder. These broadened disturbances are then propagated in a wave-like manner throughout the outer hyperbolic region. The result is a smoothly varying near symmetrical acoustic signature in the far-field.

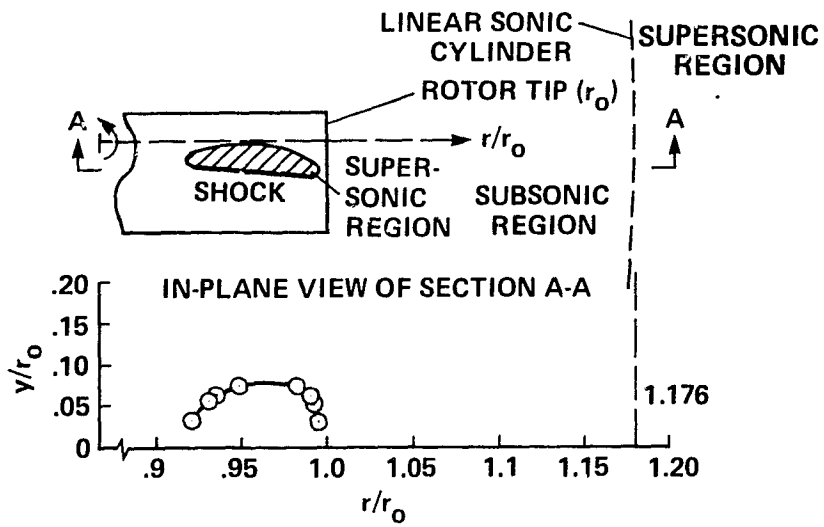

Figure 4. Top and aft views of shock boundaries of a rotor, $M_{tip} = 0.85$.

The competing phenomena become even more interesting when the undisturbed free-stream tip Mach number of the rotor (M_{tip}) is increased to 0.88 (Fig. 5). The inner supersonic (or hyperbolic) region grows and extends off the tip of the rotor — again being driven by local aerodynamic nonlinearities. At the same time, the higher free-stream tip Mach number of

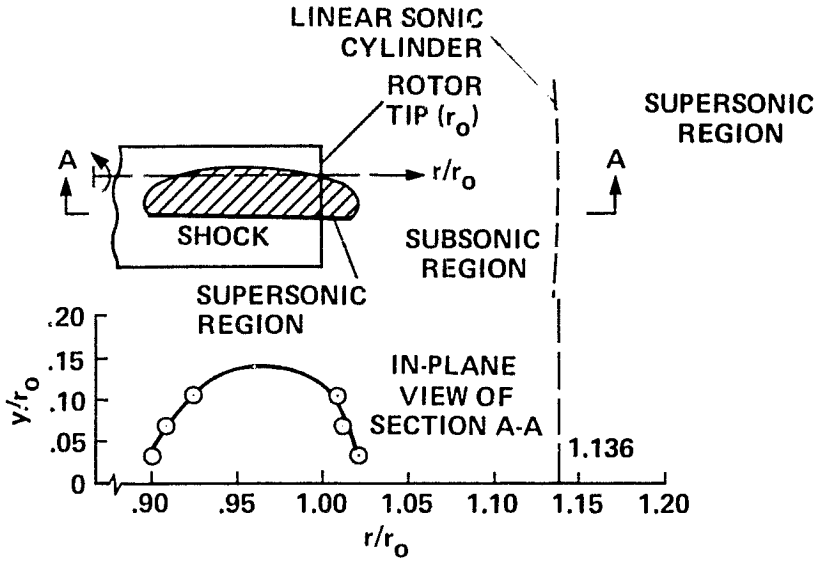

Figure 5. Top and aft views of shock boundaries of a rotor, $M_{tip} = 0.88$.

the rotor decreases the radius of the sonic cylinder, thus moving the outer hyperbolic region toward the rotor tip. In addition, the proximity of the linear sonic cylinder to the blade tip introduces aerodynamic nonlinearities. These tend to warp the sonic cylinder inward, bringing the two hyperbolic regions even closer together. However, the hyperbolic regions do not overlap, thus insuring that locally generated waves in the inner region do not propagate along characteristics to the hyperbolic far-field. Instead, the wave-like disturbances are forced to pass through a small elliptic region where they are broadened before entering the outer hyperbolic region for propagation to the far-field. The resulting acoustic signature becomes more sawtoothed in character, but does not contain radiating shocks.

The last and most interesting condition, in which the local free-stream tip Mach number is increased to 0.9, is sketched in Figure 6. The

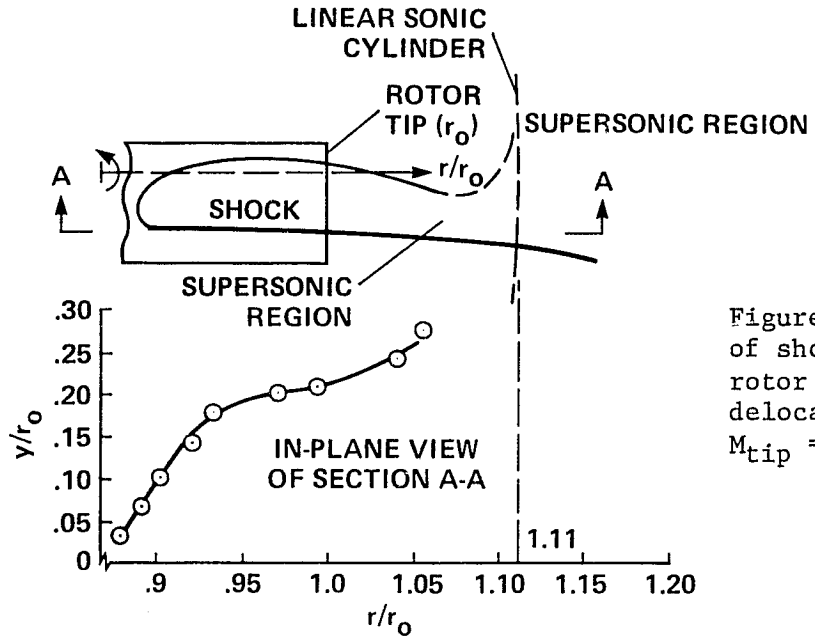

Figure 6. Top and aft views of shock boundaries of a rotor — the development of delocalization phenomenon, $M_{tip} = 0.9$.

localized inner hyperbolic and outer hyperbolic regions connect off the blade tip, forming one continuous supersonic region ($M_\ell > 1.0$). In this case, shock waves that are generated on the surface of the rotor now propagate uninterruptedly in a radially outward characteristic direction to the acoustic far-field. The resulting delocalization phenomenon is quite striking, for the character and the intensity of the acoustic signature change dramatically. At all three of these conditions, measured values of local Mach number support and explain the phenomenon of "transonic delocalization."

3. THE QUADRUPOLE APPROXIMATION AND THE ACOUSTIC FIELD

Although the phenomenon of delocalization has been explained by simply looking at the coefficient of ϕ_{99} in Equation (2), predicting the radiating acoustic field is another matter. The explanations presented are themselves functions of either measured or calculated flow properties. In essence, a near-field description of the aerodynamic flow field is required before the events in the acoustic far-field can be explained. Even then, acoustic nonlinearities in Equation (2) may alter the waveform of the propagating wave (Refs. 11, 13). Precise calculations of the radiating sound field are dependent on the full solution of the nonlinear potential equation (Eq. (2)).

On the other hand, the successful explanation of the delocalization phenomenon suggests that local aerodynamic nonlinearities strongly influence the acoustic radiation problem. Therefore, a logical step in the calculation of the acoustic field is the incorporation of the near-field aerodynamic nonlinearities in the acoustic radiation equation.

At least two alternative ways of implementing this idea have been presented in the literature. One recently proposed method (Ref. 12) maps the nonlinear near-field to a nonrotating control surface where Kirchoff's theorem is applied. As reported, the control surface must be chosen to be large enough to capture the nonlinear aerodynamic behavior of the problem, but not to be so large as to make numerical computation impractical. Initial calculations, using this procedure coupled with an existing near-field numerical code, have shown improvement in peak amplitude levels, but not much improvement in waveform characteristics above the delocalization Mach number. As discussed in Reference 12, this is most likely due to the numerical insensitivity of the transonic code at the boundary of the nonrotating control surface.

The second method employs the well-known "acoustic analogy" procedures to evaluate the volume distributions of local aerodynamic nonlinearities or quadrupoles (Refs. 1, 5, 17). This approach is utilized in this paper together with an accurate estimation of the local three-dimensional nonlinear aerodynamic flow field. It was first attempted in Reference 1 for high-speed helicopter impulsive noise by approximating the quadrupole term, using two-dimensional Prandtl-Glauert aerodynamic theory. Although small improvements in amplitude were noted, there remained major discrepancies between theory and experiment. The authors of Reference 5 performed a similar calculation for a transonic propeller using two-dimensional transonic codes for input; they reported better agreement in amplitude but poor agreement in pulse shape. Three-dimensional transonic aerodynamics were included in Reference 17 for the hovering helicopter rotor, and the results were more impressive. However, the limitation of integration

region for the quadrupole term and the omission of shock terms caused poor agreement between pulse shape and theory near or above the delocalization Mach number. In this paper, these latter two restrictions are removed from the quadrupole approximation in the transonic acoustic field.

The analysis begins with the well-known Ffowcs Williams and Hawkings formulation (Ref. 7), in which the sound radiated by surfaces in motion is expressed as the integral equation:

$$4\pi a_0^2 p'(\bar{x},t) = \frac{\partial}{\partial t}\int\left[\frac{\rho_0 u_n}{R|1-M_R|}\right]dS - \frac{\partial}{\partial x_i}\int\left[\frac{p_{ij}n_j}{R|1-M_R|}\right]dS$$

$$+ \frac{\partial^2}{\partial x_i \partial x_j}\int\left[\frac{T_{ij}}{R|1-M_R|}\right]dV \qquad (8)$$

where

$$T_{ij} \equiv \rho u_i u_j + p_{ij} - a_0^2 \rho \delta_{ij}$$

and standard notation is assumed.

The first term in Equation (8) is the linear thickness contribution to the radiated noise. This surface integral has been evaluated by many authors, but their efforts yielded the generally poor agreement with experiment discussed previously. The second term, also a surface integration over the blade, can be classified as either a linear or a nonlinear term, depending on how the surface pressure is approximated. However, for most of the in-plane computations reported here, its contribution to the radiated noise field is small and thus has been neglected. A strict evaluation of the quadrupole (third) term in Equation (8) requires a volume integration over all space. However, the interest in this paper is in capturing those nonlinear aerodynamic terms that may govern the acoustic radiation problem. Therefore the evaluation of the quadrupole term is confined to a volume integration within the aerodynamic nonlinear flow field of the blade.

The quadrupole term assumes a simpler form if we restrict our attention to the acoustic far-field. Then the spatial differentiations can be easily converted to time differentiations. The last term of Equation (8) becomes

$$\frac{\partial^2}{\partial x_i \partial x_j}\int_V\left[\frac{T_{ij}}{R|1-M_R|}\right]dV \cong \frac{1}{a_0^2}\frac{\partial^2}{\partial t^2}\int_V\left[\frac{T_{RR}}{R|1-M_R|}\right]dV \qquad (9)$$

where $T_{RR} = T_{ij}\hat{R}_i \cdot \hat{R}_j$, and $\hat{R}$ is the unit vector from the source at the retarded time to an observer in the acoustic far-field. It is known from transonic computations and experimentation that the primary quadrupole regions are confined within a few chord lengths normal to the rotor plane.

For in-plane far-field radiation, the unit vector $\hat{R}$ is nearly in the blade rotational plane and is nearly parallel to the blade chordwise direction when the acoustic pressure reaches its peak level. If isentropic flow is assumed and the perturbation velocities are measured in the coordinate system given in Figure 2, T_{RR} becomes

$$T_{RR} = \rho_0 \left(v_\theta^2 \cos^2\theta + 2 v_r v_\theta \cos\theta \sin\theta + v_r^2 \sin^2\theta \right)$$

$$+ \frac{\gamma - 1}{2} \rho_0 \left(\frac{\omega r}{a_0} \right)^2 v_\theta^2 \qquad (10)$$

where the z component of the perturbation velocity does not appear because of the choice of an in-plane far-field microphone position. For simplicity in the resulting calculations, it has also been assumed that $\sin\theta \approx 0$ and that $u \approx v_\theta$ near the integration region of interest. This is true as long as the quadrupole field is in fact localized to a region near the rotor tip. Then, Equation (10) becomes

$$T_{RR} \approx \rho_0 u^2 \cos^2\theta + \frac{\gamma - 1}{2} \rho_0 \left(\frac{\omega r}{a_0} \right)^2 u^2 \qquad (11)$$

where u represents the perturbation velocity along the blade chord and ωr is the free-stream velocity of the point in the flow field being evaluated. The two terms represented in Equation (10) arise from similar properties of the flow already discussed in the potential formulation (Eq. (4)). Changes in the local speed of sound and local streamwise perturbation nonlinearities are included although the equation forms do not permit a one-to-one correspondence of terms.

Equations (8), (9), and (11) describe the nonlinear far-field acoustic radiation of the transonic hovering rotor. For subsonic tip Mach numbers, numerical evaluation of the surface integrals presents no real problems. However, the volume integration of quadrupoles is not as straightforward.

As discussed previously, the accuracy of this nonlinear formulation is totally dependent on the detailed knowledge of the flow field surrounding the blade. In this paper, the flow fields of interest were computed by the three-dimensional transonic numerical code described in Reference 15. This code solves the near-field transonic small-disturbance potential equation in a blade-fixed reference frame. The solution uses a conservative, mixed-difference relaxation scheme. Because this code was developed to predict blade-surface aerodynamics, some simplifying assumptions were made to Equation (2) -- namely, the nonlinearities known to be small near the blade surface were neglected. In particular, the terms $2\omega\phi_r\phi_{r\theta}$ and $2\omega\phi_z\phi_{z\theta}$ on the left-hand side and the factor $(\gamma - 1)\omega\phi_\theta$ on the right-hand side of Equation (2) were not programmed.

The nature of the calculated chordwise pressure distributions as a function of blade radius is shown in Figure 7 for a tip Mach number of 0.9 at zero angle of attack. On the blade surface, a shock wave forms at about 90% of the span and persists over the outer portions of the blade and beyond. These calculated pressure distributions are consistent with the experimentally sketched flow regions of Figure 6. The maximum value of shock strength is calculated to occur at 95% radius. It is also important to note that the shocks that are calculated with this code do not look like measured shock waves. The numerical solution has built into it a numerical viscosity which tends to smooth discontinuities over several mesh points. This tends to smooth the final acoustic waveforms to some degree.

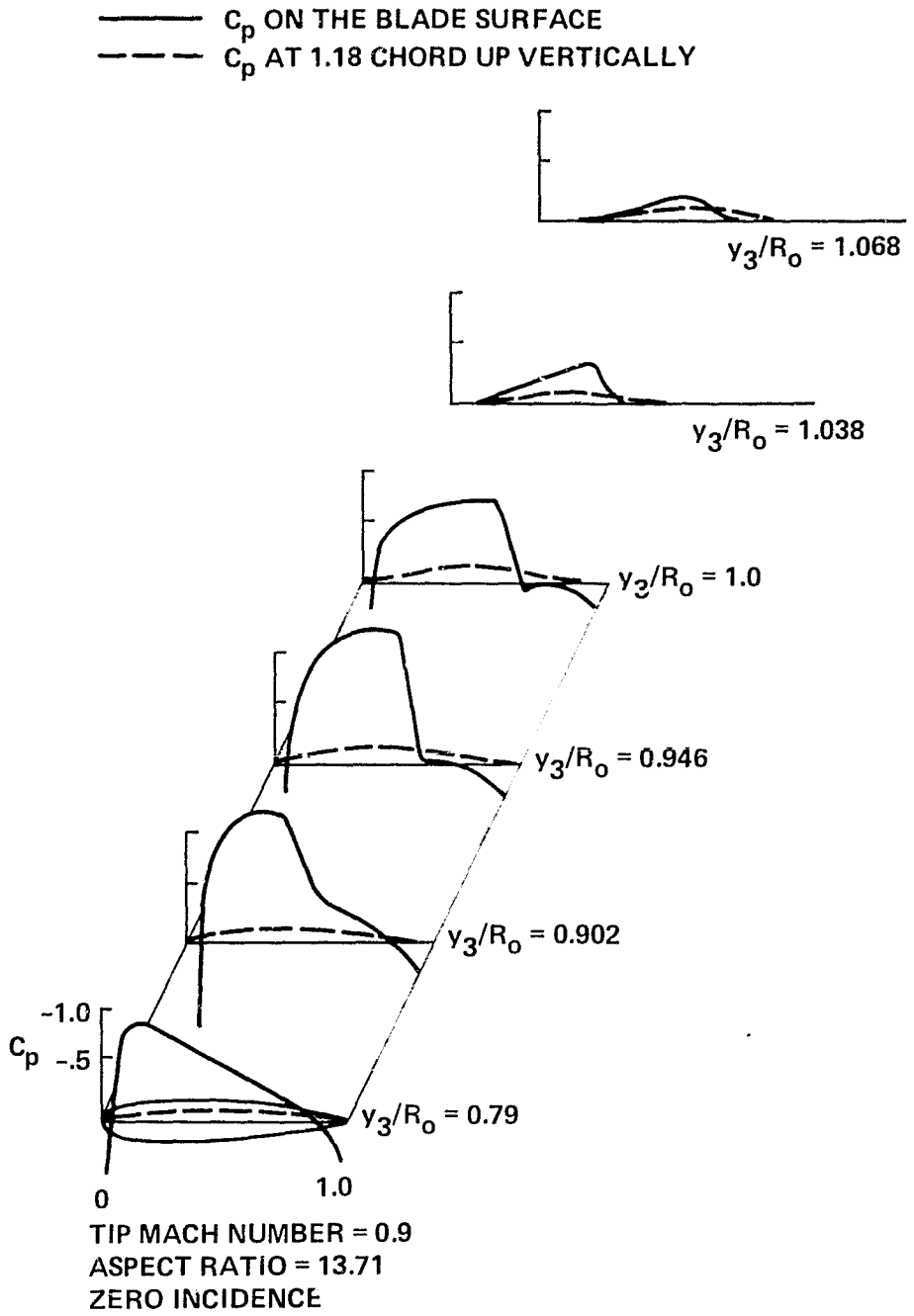

Figure 7. C_p distribution on the blade surface and at 1.18 chords up, aspect ratio = 13.7, NACA 0012, near zero angle of attack, M_{tip} = 0.9.

The vertical extent of the local flow field is shown in Figure 8 for the 95% span location. The rapid decay in disturbance velocity u has been confirmed by experiment. However, as indicated in Reference 17, the decay with vertical distance from the airfoil is much faster than with two-dimensional transonic theory, but much slower than with linear calculations. The faster decay of three-dimensional transonics is caused by tip relief. This figure illustrates that the blade tip region is governed by local nonlinear three-dimensional transonic efforts and must be calculated accordingly.

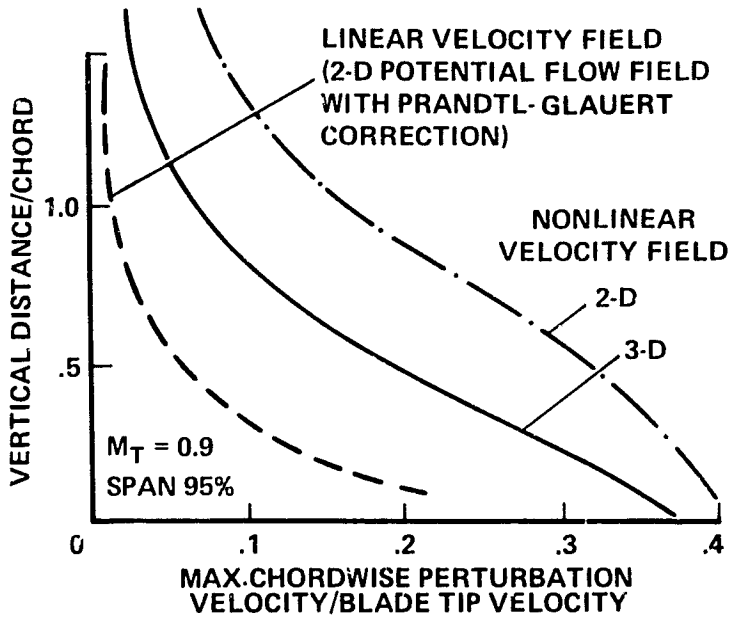

Figure 8. Vertical extent of the local flow field, $M_{tip} = 0.9$.

The final problem in the evaluation of the quadrupole integral is the development of a calculation procedure for Equations (8), (9), and (11) that is valid when $M_R = 1.0$. This problem occurs when the volume integration is extended up to and beyond the linearized sonic cylinder. The integrand in Equation (9) then contains the product of two terms which compete to decide the eventual magnitude of the quadrupole radiation. The first is the decaying source field represented by the T_{RR} term in Equation (9). This is multiplied by the $1/|1 - M_R|$ term which goes to ∞ as M_R approaches 1. Fortunately, the singularity is integrable, but it must be handled quite carefully. In this paper the acoustic planform technique was chosen to perform the numerical integration near $M_R = 1.0$. A complete discussion of the procedures and pertinent references is given in the Appendix.

Equation (11) governs the magnitude of the quadrupole source strength, T_{RR}. For an observer in the acoustic far-field, and for an integration region confined near the blade tip, all effective source points normal to the rotor plane will arrive at the same retarded time. Therefore it is possible to integrate u^2 in the z direction and effectively collapse the quadrupole volume integration to a surface integral in the rotor plane (Ref. 17). The resulting integration for the model rotor operating at near zero thrust at a hover tip Mach number of 0.9 is shown in Figure 9 for several radial stations. The integral $\int u^2\, dz$ is the largest at about $r/r_0 = 0.95$ and decreases both inboard and outboard of this point. The monotonic decrease in amplitude out past the tip to beyond the linear sonic circle suggests that quadrupole sources die quickly. However, the ultimate strength of the quadrupole term is dependent on the integration over an effective planform of the product of $\int u^2\, dz$ and $1/|1 - M_R|$. Because $1/|1 - M_R|$ is singular when $M_R = 1.0$, the net quadrupole integration is weighted heavily near the sonic circle. The resulting contributions to the acoustic field are shown in Figure 10 for the same hovering rotor at near zero thrust. As shown, the dominant integration region for the quadrupole

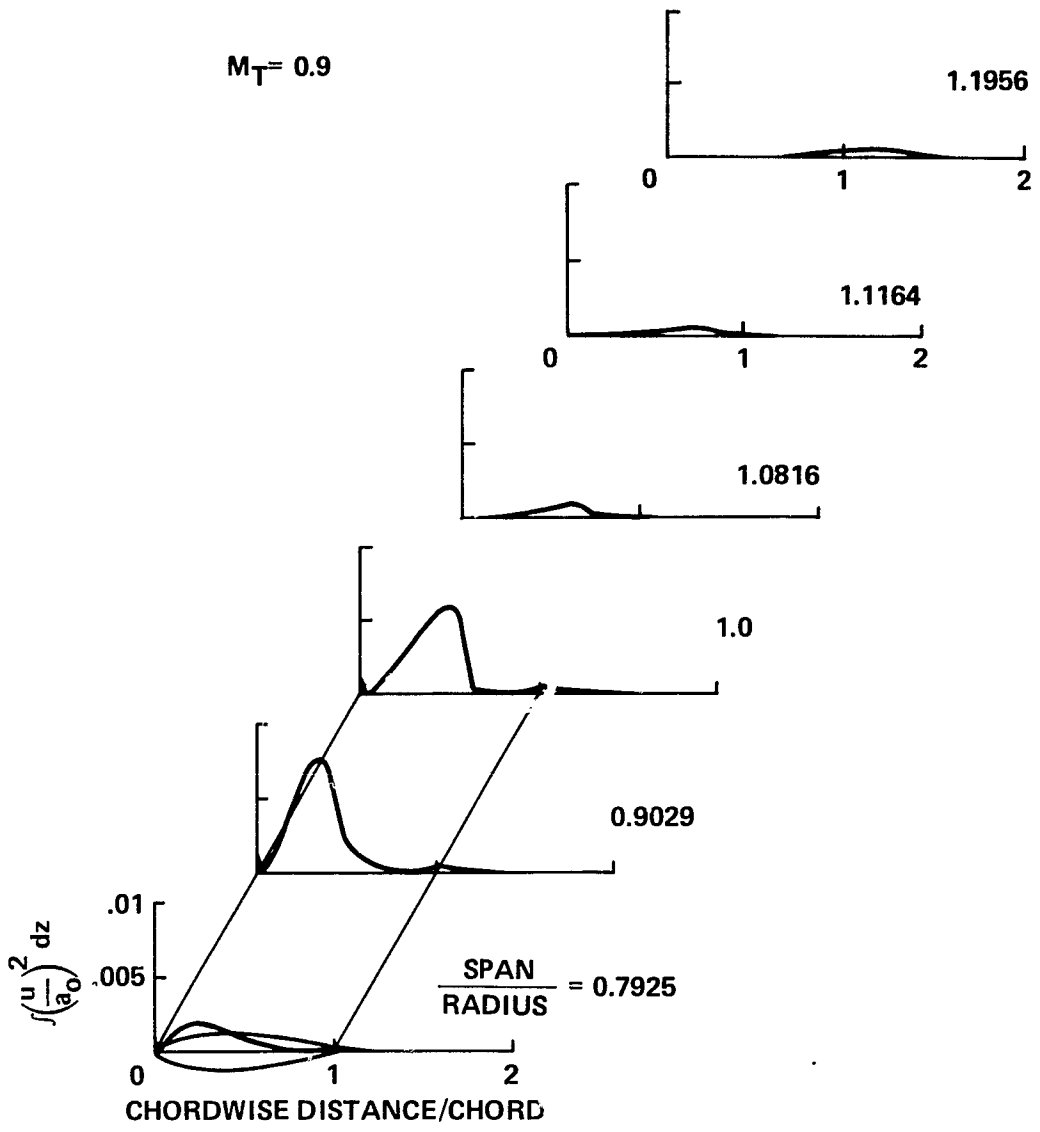

Figure 9. Quadrapole source strength as a function of r/r_o for M_{tip} = 0.9.

term is between the rotor blade tip and the linear sonic circle. The figure also illustrates how the shape of the quadrupole term changes near a hover tip Mach number of 0.9 for the UH-1H model rotor. At these high tip speeds, the shape of the quadrupole term is strongly influenced by the shape of $\int u^2\, dz$ near the sonic circle. The resulting waveform becomes sawtoothed in character because the governing equations are nearly hyperbolic in character in this region. The structure of the $\int u^2\, dz$ field is nearly preserved, yielding a shock-like quadrupole waveform in the acoustic far-field.

This does not happen at lower hover tip Mach numbers. The amplitude of the $\int u^2\, dz$ field dies away rapidly causing the quadrupole integral to be dominated by the linear elliptic region. Here, no wave-like structure is possible and the structure of $\int u^2\, dz$ is smoothed in the amplification process, producing nearly symmetrical pressure time histories.

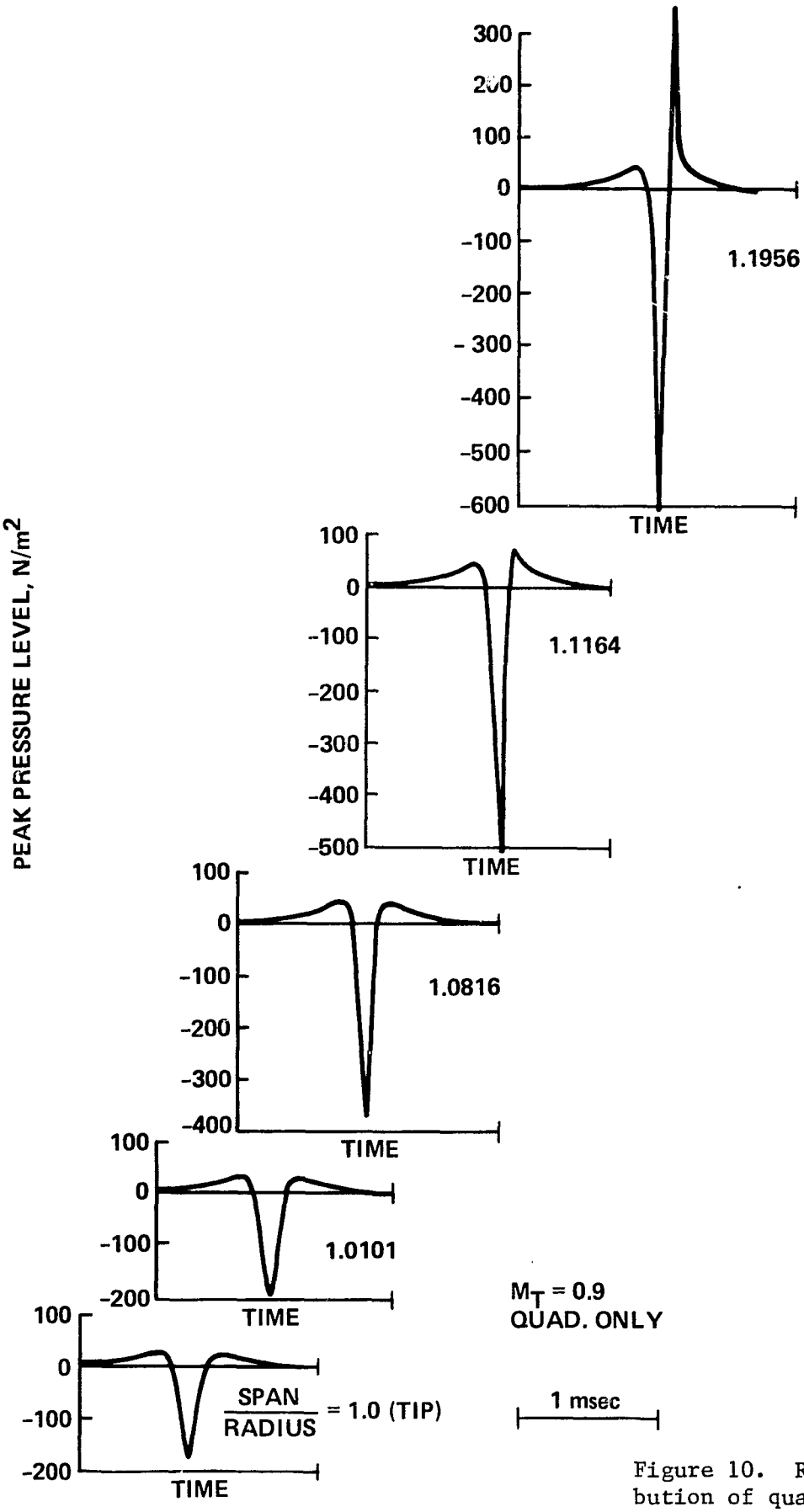

Figure 10. Radial contribution of quadrapole radiation.

4. COMPARISON WITH EXPERIMENT

An evaluation of the overall prediction accuracy is presented below by a comparison with data presented in Reference 2. In that test, a 1/7 scale model of a UH-1H helicopter (NACA 0012 airfoil with 10.9° twist and with no twist) was run at nearly zero thrust at transonic tip Mach numbers from 0.8 to 1.0 in hover in an anechoic hover chamber. Microphones located in the plane of the rotor recorded the radiated noise.

Figure 11 presents the monopole and quadrupole contributions to the radiated noise at $M_{tip} = 0.8$. As discussed previously, at these low tip Mach numbers the monopole contribution to the radiated in-plane far-field noise underpredicts the magnitude of the measured data (Ref. 2), but accurately predicts the pulse shape (Fig. 11a). The quadrupole contribution is of an almost similar shape (Fig. 11b) and helps improve the correlation with experiment (Figs. 11c, 11d) to nearly acceptable levels.

As the hover tip Mach number is increased to 0.88 (Fig. 12) the monopole and quadrupole terms (Figs. 12a, 12b) become equally large in magnitude. More importantly, however, the shape of the quadrupole term begins to change from a near-symmetrical to an asymmetrical character. This is noted on the pressure recovery side of the quadrupole calculation

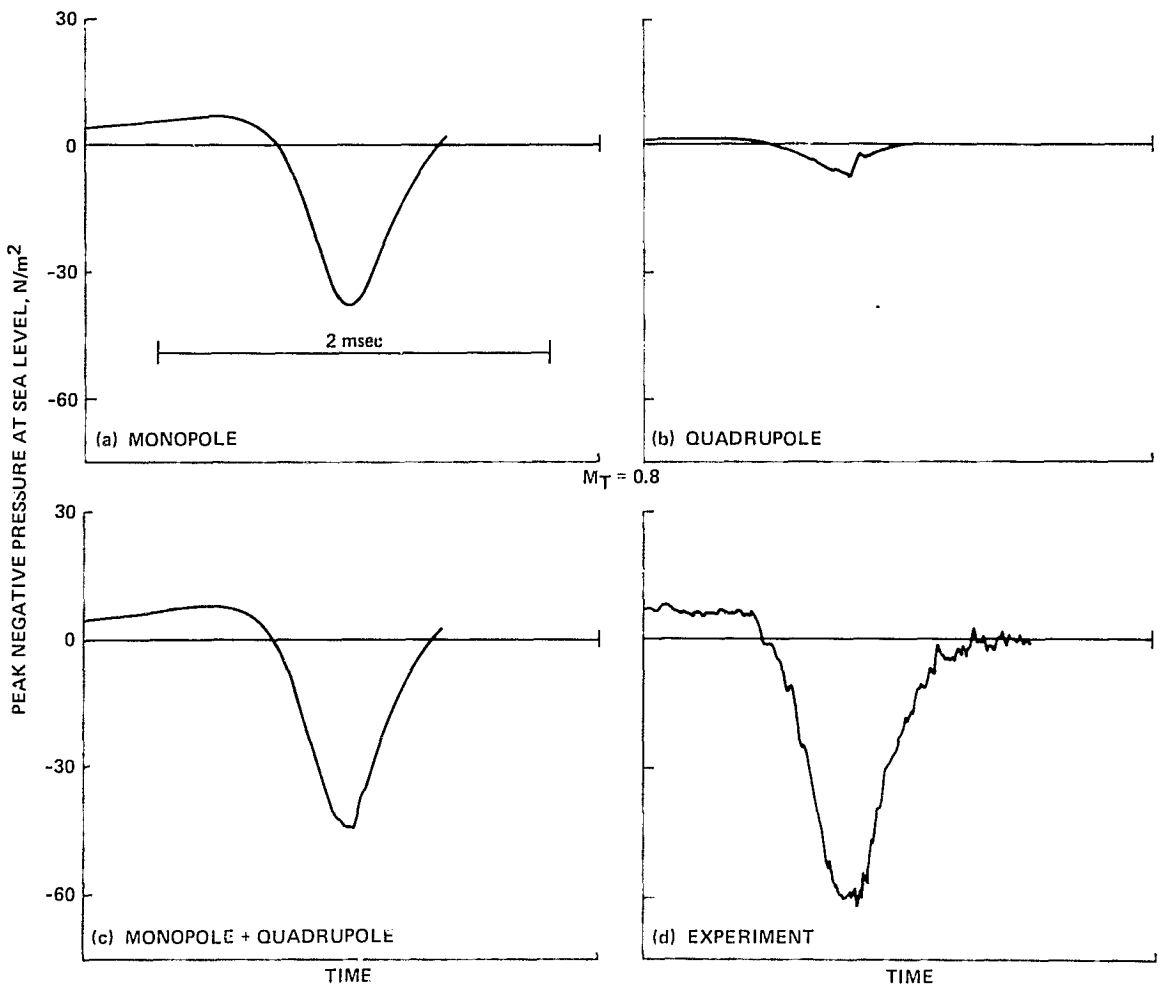

Figure 11. Theory-experiment comparison, $M_{tip} = 0.8$.

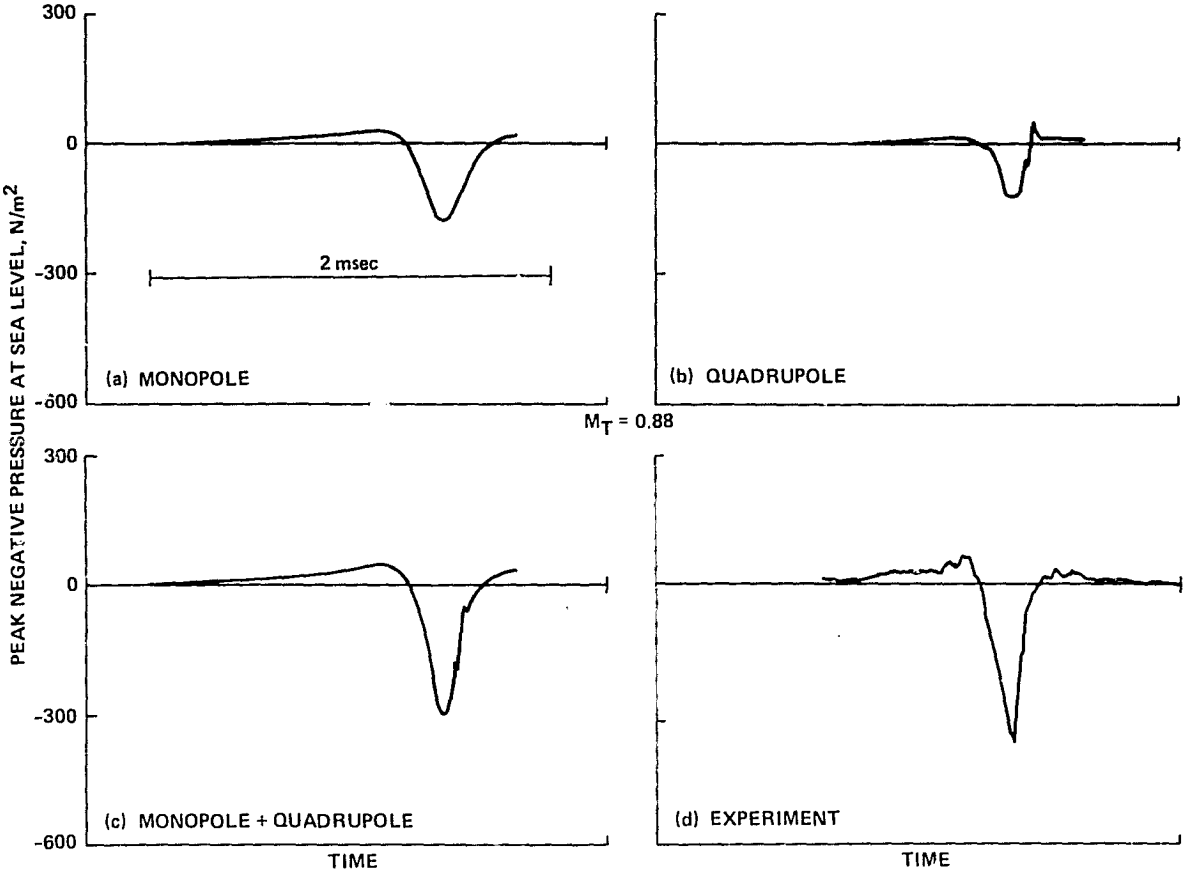

Figure 12. Theory-experiment comparison, M_{tip} = 0.88.

and is a direct result of including the local shock structure of the flow field in the numerical calculation. When the monopole and quadrupole contributions are added, good correlation in amplitude and pulse shape is observed (Figs. 12c, 12d). The overall shape of theory and experiment are still basically symmetrical in character, but the local shock structure of the transonic flow field is acting to destroy this symmetry.

At the slightly higher hover tip Mach number of 0.90, localized transonic effects cause large changes to the radiated noise field (Fig. 13). Although the linear term (monopole, Fig. 13a) remains quite symmetrical in shape and substantially underpredicts the measured data, the nonlinear (quadrupole, Fig. 13b) term changes shape dramatically and increases in amplitude. This is a reflection of the fact that local shocks are propagating to the far acoustic field ("delocalization" in Ref. 17). When the monopole and quadrupole terms are compared with experimental data (Figs. 13c, 13d), good agreement in pulse shape is observed. To the authors' knowledge, this is the first time calculated pulse shapes have compared favorably with measured data for a rotor operating near the "delocalization" Mach number.

The relative accuracy with which the peak negative amplitude of the high-speed impulsive noise phenomenon can be predicted is illustrated in Figure 14. Much better agreement between theory and experiment is demonstrated for Mach numbers of up to 0.9. At $M_{tip} \geq 0.9$, amplitudes are overpredicted. This result is related to the sensitivity of this approach to perturbation velocities near the linear sonic circle and to the accuracy with which existing transonic near-field codes can predict these velocities.

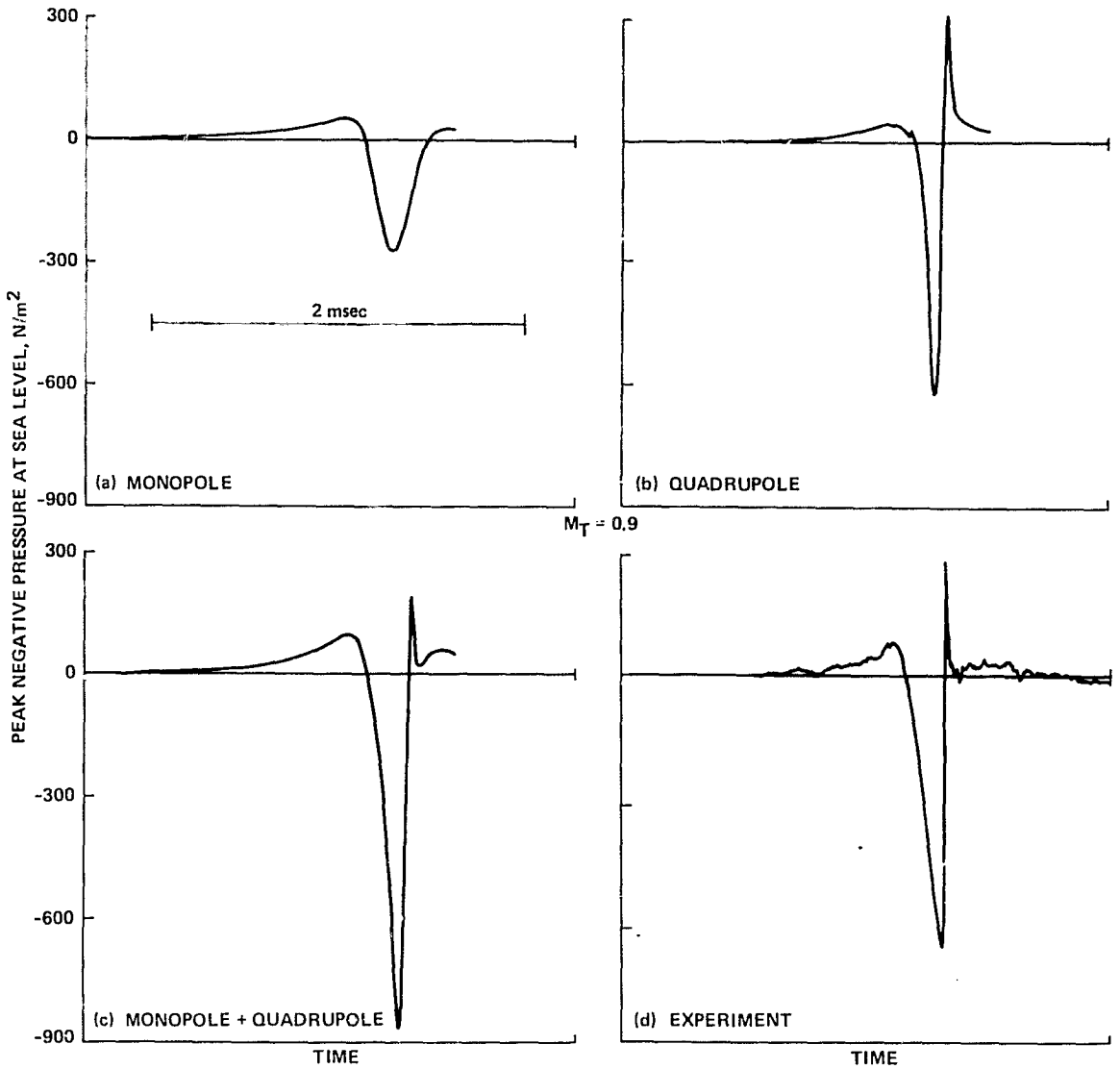

Figure 13. Theory-experiment comparison, M_{tip} = 0.90.

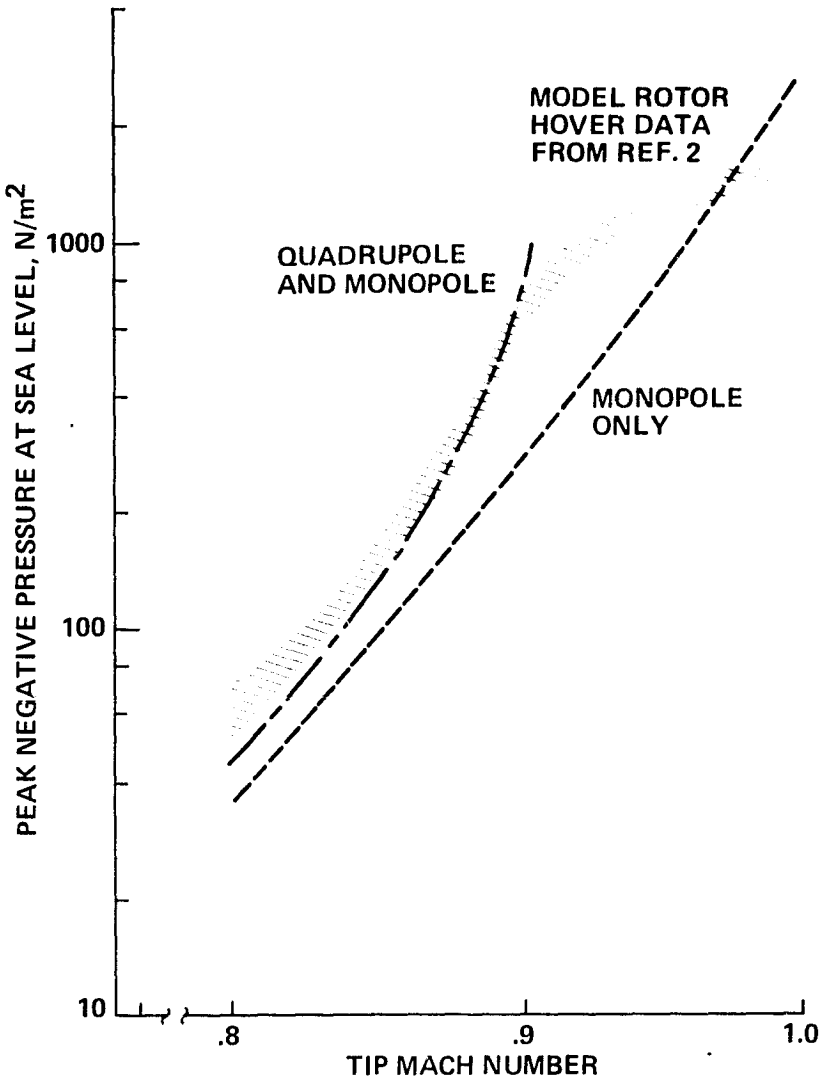

Figure 14. Comparison of theory and experiment in hover, in-plane, r/D = 1.5.

5. SOME FURTHER OBSERVATIONS

Some insight into why overprediction of the acoustic pulse near the "delocalization" Mach number is likely can be gained from Figure 15. In this figure, peak values of measured horizontal perturbation velocities are compared with the local transonic potential code used in this paper for $M_{tip} = 0.9$. Inward from the tip of the rotor blade comparison with experiment is quite good; however, near the linear sonic cylinder where the quadrupole contributions to the radiated noise are large, theory and experiment diverge. It is quite likely that the overestimation of the transonic perturbation velocity in this region causes the quadrupole contribution (which squares the error) to become too large. A transonic code that incorporates all of the near-field nonlinearities should help the correlation of this acoustic theory with experiment at the higher transonic tip speeds.

A plot of the torque coefficient versus hover tip Mach number is given in Figure 16 for the untwisted model rotor (Ref. 2) at near zero

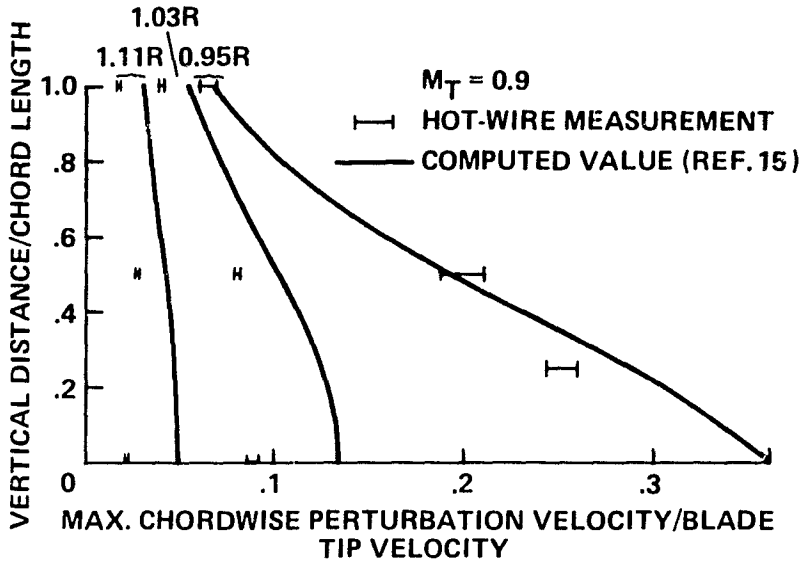

Figure 15. Comparison of maximum measured and provided chordwise perturbation velocities.

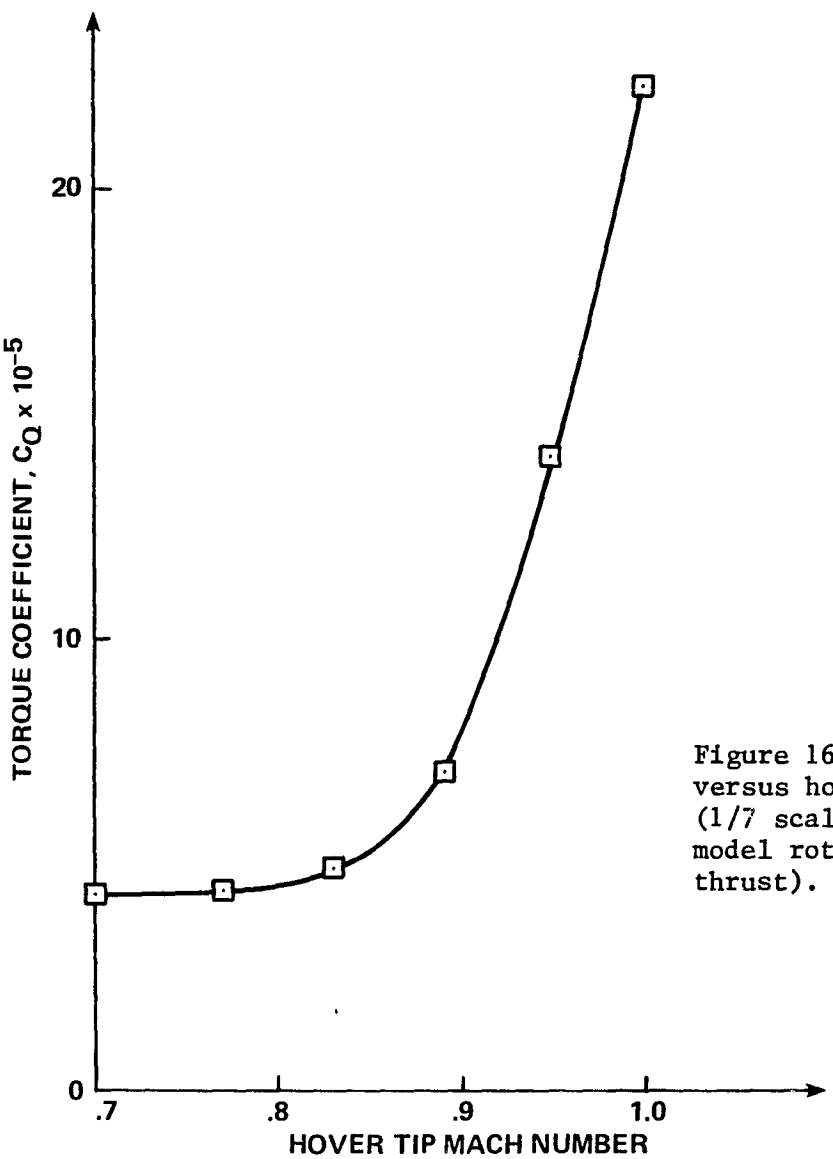

Figure 16. Torque coefficient versus hover tip Mach number (1/7 scale UH-1H untwisted model rotor at near zero thrust).

thrust. The resulting curve increases sharply, defining a point at a hover tip Mach number of about 0.85 that might be considered to be the onset of "drag divergence." This is in contrast to the phenomenon of "delocalization," which occurs at $M_{tip} = 0.9$ for this model rotor. It is probable that the two events are related, but the experimental and theoretical evidence to date does not explicitly connect drag rise with radiated noise.

6. CONCLUSIONS

Inclusion of the quadrupole terms in the numerical evaluation of the Ffowcs Williams and Hawkings integral equation improves the comparison with measured data for high-speed helicopter rotors operating at tip Mach numbers from 0.8 to 0.9. The predicted waveform closely matches the measured data. At low-tip Mach numbers ($M_{tip} = 0.8$), nearly symmetrical pulse shapes are predicted and measured while at the delocalization Mach number ($M_{tip} = 0.9$) sawtoothed shock-like waveforms are predicted and measured. However, at Mach numbers greater than 0.9, theory tends to overpredict measured peak negative amplitudes.

The changing character of the acoustic waveform depends critically on the local three-dimensional transonic flow field surrounding the blade tip. If the local supersonic region surrounding the blade is bounded by a subsonic cylindrical region, the waveform remains near symmetric in character. However, at higher Mach numbers ($M_{tip} = 0.9$), when the local supersonic region connects with an outer hyperbolic region, the waveform becomes sawtoothed and local shocks propagate (delocalize) to the acoustic far-field.

Predicted acoustic waveforms are dependent upon accurate knowledge of the near-field perturbation velocity field near the blade tip. For the present paper, this near-field is computed using a small disturbance code which incorporates near-field aerodynamic nonlinearities near the blade surface. Measurements of peak perturbation velocities indicate that this small disturbance transonic theory is in good agreement in-board of the tip region but becomes less accurate (overpredicts) off the blade tip. This is thought to be one reason why the quadrupole acoustic formulation tends to overpredict measured values at Mach numbers greater than 0.9. It is doubtful that quantitative prediction of far-field transonic rotor noise at Mach numbers greater than 0.9 can be attempted until the transonic potential equation is solved over regions of larger radial extent than the equation has dealt with to date. It is clear that local transonic aerodynamics strongly influence the high-speed rotor's acoustic far-field. In the next few years, design changes based on this new understanding should help reduce the radiated noise.

APPENDIX

The integral equation for the volume displacement effect is shown as follows (Ref. 7):

$$4\pi a_0^2 \rho'(\bar{x},t) = \frac{\partial}{\partial t} \int_{-\infty}^{t} \iiint_{-\infty}^{\infty} \frac{Q(\bar{y},\tau)}{R} \delta(f) |\nabla f| \delta(g) d\bar{y}\, d\tau \qquad \text{(A1)}$$

where

$$Q(\bar{y},\tau) = \rho_0 v_n$$

$$g = \tau - t + \frac{r}{a_0} \tag{A2}$$

τ = retarded time $\qquad R = |\bar{x} - \bar{y}|$

t = observer time $\qquad \bar{x}$ = observer position vector

$f = 0$: body surface $\qquad \bar{y}$ = source position vector

Since the intervals of the integrals are infinite, the order of integration can be interchanged. Then Equation (A1) becomes

$$4\pi a_0^2 \rho'(\bar{x},t) = \frac{\partial}{\partial t} \iiint_{-\infty}^{\infty} \frac{Q(\bar{y},\tau)}{R} \delta\{f(\bar{y},\tau)\} |\nabla f(\bar{y},\tau)| d\bar{y} \tag{A3}$$

where

$$\tau = t - \frac{R}{a_0}$$

If the $\bar{y}$ coordinate system is changed to the $\bar{\xi}$ coordinate system, such that the ξ_1 axis is perpendicular to the surface $f(\bar{y},\tau) = 0$, and the ξ_2,ξ_3 axes are on that same surface (see sketch), Equation (A3) becomes

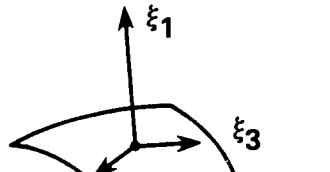

$$4\pi a_0^2 \rho'(\bar{x},t) = \frac{\partial}{\partial t} \iiint_{-\infty}^{\infty} \frac{Q(\bar{\xi},\tau)}{R} \delta\{f(\bar{\xi},\tau)\} |\nabla f(\bar{\xi},\tau)| J(\bar{y},\bar{\xi}) d\bar{\xi} \tag{A4}$$

The Jacobian $J(\bar{y},\bar{\xi})$ between coordinate systems $\bar{y}$ and $\bar{\xi}$ is expressed as follows

$$J(\bar{y},\bar{\xi}) = \frac{1}{|\nabla f| \alpha}$$

where

$$\alpha = \left\{1 + 2 \frac{v_n}{a_0} \hat{R}_i \cdot \bar{n} + \left(\frac{v_n}{a_0}\right)^2\right\}^{1/2}$$

This expression is obtained as follows. Define a function F such that

$$F = f(\bar{\xi},\tau)$$

Then

$$\nabla F = \nabla_\xi f + \frac{\partial f}{\partial t}\frac{\partial \tau}{\partial \xi}$$

$$= \nabla_\xi f - \bar{v}\cdot\bar{n}|\nabla f|\left(\frac{-1}{a_0}\right)\hat{R}_i$$

$$= |\nabla_\xi f|\left\{\bar{n} + \frac{\bar{v}\cdot\bar{n}}{a_0}\hat{R}_i\right\}$$

Also,

$$|\nabla F| = |\nabla_\xi f|\left\{1 + 2\frac{v_n}{a_0}\hat{R}_i\cdot\bar{n} + \left(\frac{v_n}{a_0}\right)^2\right\}^{1/2}$$

$$= |\nabla_\xi f|\alpha$$

Therefore,

$$J = \frac{1}{|\nabla F|} = \frac{1}{|\nabla f|\alpha}$$

Now Equation (A4) becomes as follows with the Jacobian $J(\bar{y},\xi)$

$$4\pi a_0^2\rho'(\bar{x},t) = \frac{\partial}{\partial t}\iiint_{-\infty}^{\infty}\frac{Q(\bar{\xi},\tau)}{R\alpha}\,\delta\{f(\bar{\xi},\tau)\}\,d\bar{\xi} \qquad \text{(A5)}$$

Since the coordinate system is defined such that ξ_1 is perpendicular to the surface defined by $f(\bar{\xi},\tau) = 0$, $d\bar{\xi}$ becomes as follows:

$$d\bar{\xi} = d\xi_1\, d\xi_2\, d\xi_3$$

$$= df\, d\xi_2\, d\xi_3$$

With this, Equation (A5) becomes

$$4\pi a_0^2\rho'(\bar{x},t) = \frac{\partial}{\partial t}\iint\frac{Q(\xi_2,\xi_3,\tau)}{R\alpha}\,d\xi_2\, d\xi_3 \qquad \text{(A6)}$$

$$S:$$

$$f(\bar{\xi},\tau) = 0$$

This is the general equation for the acoustic planform method (derived also in Ref. 8), where the integration interval covers only the area of source locations in retarded time for which signals arrive at the observer simultaneously. This is equivalent to the formulation for a collapsing sphere method (see Ref. 8). The area $S\{f(0,\xi_2,\xi_3,\tau) = 0\}$ for the integration in Equation (A6) is called the acoustic planform.

The acoustic planform changes shape depending on the radiation (component of) Mach number, M_R. For very low M_R, the acoustic planform is almost congruent with the shape of the blade planform. As M_R increases, the acoustic planform distorts, and finally breaks into multiple regions for M_R greater than 1, as shown in Figure 17. Figure 17 shows a case in which a blade is rotating in a circular path with a constant supersonic tip Mach number M_{tip}. With a supersonic tip Mach number, the radiation component of the tip Mach number M_R varies from subsonic to supersonic, and then back to subsonic speed again as the azimuthal angle increases.

The multiple regions of the acoustic planform for a supersonic M_R is explained in Figure 18.

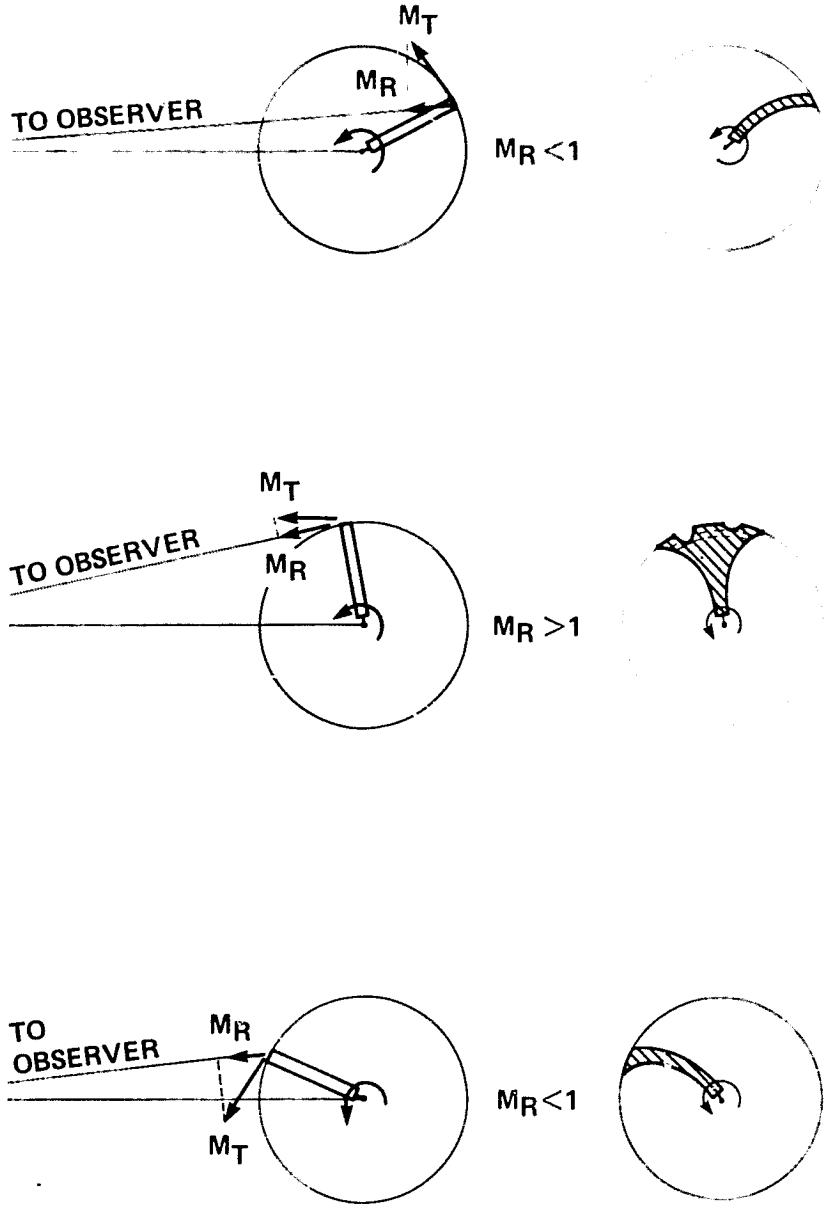

Figure 17. Physical plate and acoustical planform for a supersonic tip Mach number.

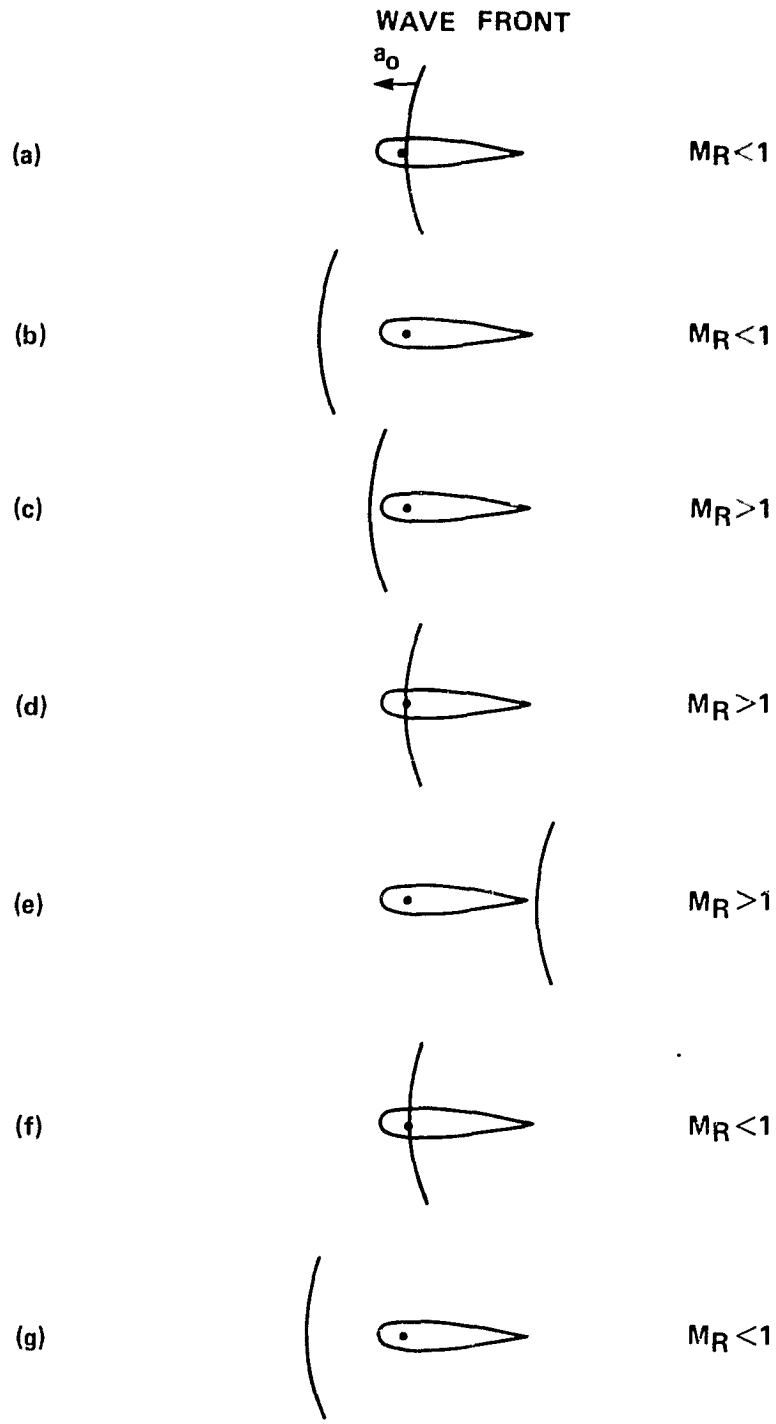

Figure 18. Relative position between wavefront and blade.

1. At $t = 0$ a sound wave is generated; because the speed of sound is faster than the blade motion M_R, the wavefront moves ahead of the blade (see Figs. 18a, 18b).

2. Now, the blade speeds up until M_R is greater than 1, and the blade catches up with the wavefront (Figs. 18c-18e).

3. The blade again slows down to a subsonic speed, and the wavefront now moves ahead of the blade (Figs. 18f, 18g).

During the variation of the blade M_R relative to the propagation speed of the wavefront, the wavefront can interact with a particular point on the airfoil one, two, or three times, depending on the value of the airfoil M_R.

These multiple values of source positions can also be shown from the point of view of a retarded time expression. The relationship between the observer time and the retarded time is given as follows:

$$\tau = t - \frac{R}{a_0}$$

From this expression, in order for signals from two separate positions on the rotor blade to reach the observer simultaneously, the following equation should be satisfied:

$$\frac{R_1}{a_0} + \frac{\psi_1}{\omega} = \frac{R_2}{a_0} + \frac{\psi_2}{\omega}$$

where R_1 and R_2 are distances from two different sources to the observer, and ψ_1 and ψ_2 are respective azimuthal angles from the original location; ω is angular velocity.

For a given angle ψ_1, the position of the second source ψ_2 may be found by the following function:

$$F(\psi) = -\frac{\omega}{a_0}(R_1 - R_2) + \psi_2 - \psi_1 = 0 \qquad \text{(A7)}$$

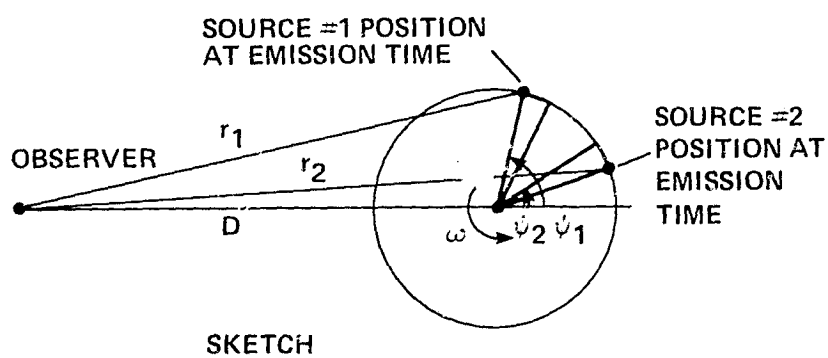

SKETCH

For a given value of ψ_1 and R_1, Figure 19 shows the graphical solution for Equation (A7). That is, for a subsonic Mach number M_R, the function F increases monotonically such that only one value for ψ_2 can be obtained (see Fig. 19a). For a supersonic case, the function F has one, two, or three roots, depending on the value of M_R; that is, one root is obtained for a subsonic M_R, two roots for $M_R = 1$, and three roots are obtained for $M_R > 1$ (see Fig. 19b).

A typical acoustic planform for a supersonic tip Mach number is shown in Figure 20, in which the leading and trailing edges corresponding

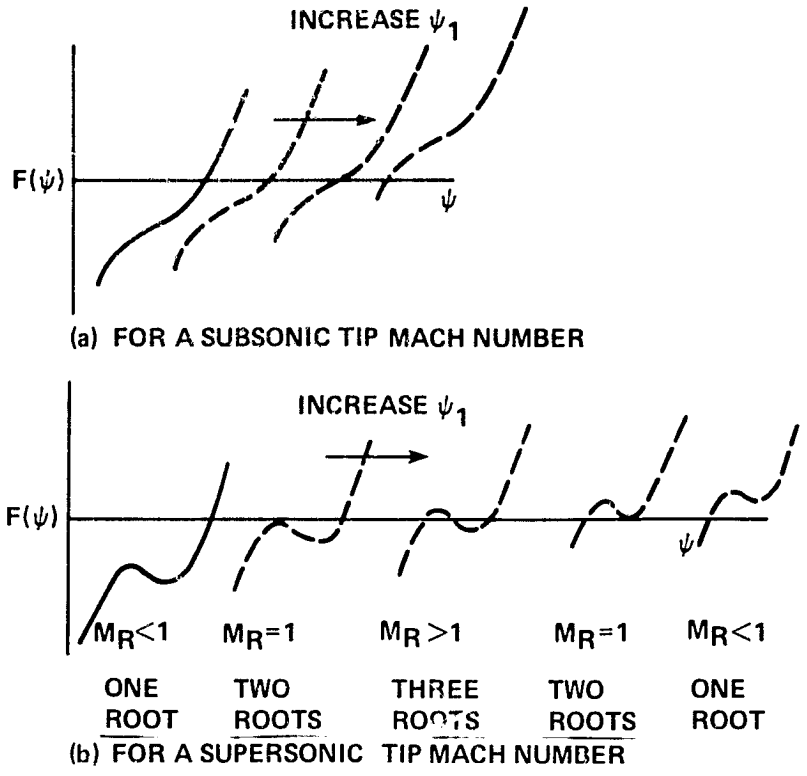

Figure 19. Number of positions of a source for subsonic and supersonic speed.

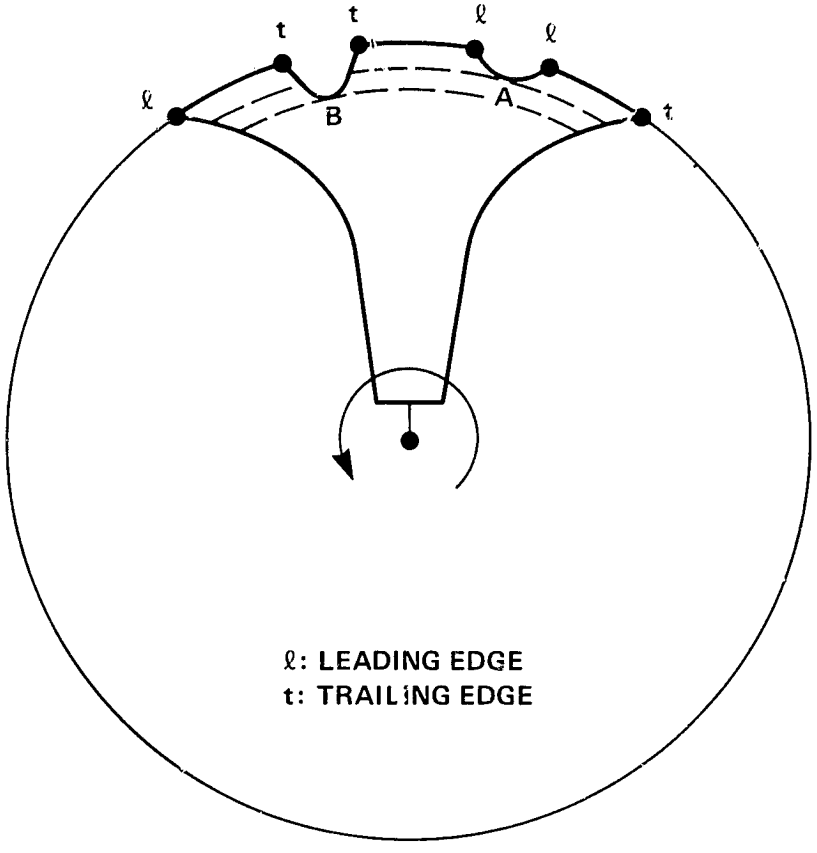

Figure 20. A typical acoustical planform for the case of the subsonic tip Mach number.

to a physical blade are shown. Two observations stand out. The first is the center portion of the planform, where the trailing edge and leading edge are reversed. This phenomenon can be explained from Figure 18. When a wavefront is ahead of an airfoil (see Fig. 18c) and the airfoil is accelerating, the wavefront first interacts with the leading edge, and then sweeps the airfoil to the trailing edge (see Figs. 18d, 18e).

A second observation is that of the two local depressions A and B shown in Figure 20. The depth of these depressions depends mainly on the magnitude of M_R. Generally, these two depths have different values. Between these different depths, the acoustic planform has only two possible regions: either one leading edge and three trailing edges or three trailing edges and one leading edge, depending on whether the local depression B is deeper or shallower than A. The outermost radial portion has three regions, and the inner radial portion has one region.

ACKNOWLEDGMENTS

We thank several of our colleagues at the Aeromechanics Laboratory for their unselfish contributions to this effort. Dr. F. Caradonna provided all of the transonic near-field numerical data shown in this paper, and Ms. Georgene Laub and Mr. D. Boxwell helped reduce much of the experimental data. We thank Mr. H. Andrew Morse for his consistent and untiring support. We also owe a special thanks to Prof. M. Isom of the Polytechnical Institute of New York for many fruitful discussions and guidance.

REFERENCES

1. F. H. Schmitz, Y. H. Yu. Theoretical Modeling of High-Speed Helicopter Impulsive Noise. J. American Helicopter Soc. (1979) 24 (1) 10-19.

2. D. A. Boxwell, Y. J. Yu, F. H. Schmitz. Hovering Impulsive Noise: Some Measured and Calculated Results. Vertica (1979) 3 (1) 33-45.

3. F. Farassat, P. A. Nystrom, C. E. K. Morris, Jr. A Comparison of Linear Acoustic Theory with Experimental Noise Data for a Small Scale Hovering Rotor. AIAA Paper 79-0608, Seattle, Wash., 1979.

4. A. R. George. Helicopter Noise -- State of the Art. AIAA Paper 77-1337, Atlanta, Ga., 1977.

5. D. B. Hanson, M. R. Fink. The Importance of Quadrupole Sources in Predictions of Transonic Tip Speed Propeller Noise. Presented at Spring Meeting of the Institute of Acoustics, Cambridge University, Cambridge, England, Apr. 1978.

6. M. J. Lighthill — On Sound Generated Aerodynamically. I. General Theory. Proc. R. Soc. London, Ser. A. (1955) 231, 505-514.

7. J. E. Ffowcs Williams, D. L. Hawkings — Sound Generation by Turbulence and Surfaces in Arbitrary Motion. Philos. Trans. R. Soc. London, Ser. A. (1969) 264, 321-342.

8. F. Farassat — Theory of Noise Generation from Moving Bodies with an Application to Helicopter Rotors. NASA TR R-451, 1975.

9. D. L. Hawkings, M. V. Lowson — Theory of Open Supersonic Rotor Noise. J. Sound Vib. (1974) 36 (1) 1-20.

10. F. H. Schmitz, D. A. Boxwell, C. R. Vause — High-Speed Helicopter Impulsive Noise. J. American Helicopter Soc. (1977) Oct., 28-36.

11. M. P. Isom — Some Nonlinear Problems in Transonic Helicopter Acoustics. POLY M/AE Report No. 79-19, Polytechnic Institute of New York, May 1979.

12. D. Hawkings — Noise Generation by Transonic Open Rotors. Paper 544, Westland Helicopter Limited Research, June 22, 1979.

13. M. P. Isom — Acoustic Shock Waves Generated by a Transonic Helicopter Blade. Paper 63, 36th American Helicopter Society Annual Forum, Washington, D.C., May 1980.

14. F. X. Caradonna, M. P. Isom — Numerical Calculation of Unsteady Transonic Potential Flow over Helicopter Rotor Blades. AIAA J. (1976) 14 (4) 482-488.

15. F. X. Caradonna — The Transonic Flow on a Helicopter Rotor. Ph.D. Dissertation, Stanford University, Stanford, Calif., Mar. 1978.

16. G. B. Witham — Linear and Nonlinear Waves. John Wiley and Sons, New York, 1974.

17. Y. H. Yu, F. X. Caradonna, F. H. Schmitz — The Influence of the Transonic Flow Field on High-Speed Helicopter Impulsive Noise. Paper 58, 4th European Rotorcraft and Powered Lift Aircraft Forum, Italy, 1978.